

# Towards high spatial resolution tissue-equivalent dosimetry for microbeam radiation therapy using organic semiconductors

Jessie A. Posar,<sup>a</sup> Matthew Large,<sup>a</sup> Saree Alnaghy,<sup>a</sup> Jason R. Paino,<sup>a</sup> Duncan J. Butler,<sup>b</sup> Matthew J. Griffith,<sup>c,d</sup> Sean Hood,<sup>a</sup> Michael L. F. Lerch,<sup>a</sup> Anatoly Rosenfeld,<sup>a</sup> Paul J. Sellin,<sup>e</sup> Susanna Guatelli<sup>a</sup> and Marco Petasecca<sup>a\*</sup>

Received 16 February 2021

Accepted 9 June 2021

Edited by A. Bergamaschi, Paul Scherrer Institut, Switzerland

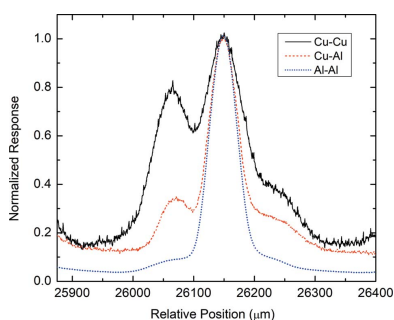
**Keywords:** organic semiconductors; microbeam radiation therapy; radiation damage; synchrotron radiation.

**Supporting information:** this article has supporting information at journals.iucr.org/s

<sup>a</sup>Centre for Medical Radiation Physics, University of Wollongong, Wollongong, NSW 2522, Australia, <sup>b</sup>Australian Radiation Protection and Nuclear Safety Agency (ARPANSA), Yallambie, Victoria 3085, Australia, <sup>c</sup>School of Aeronautical, Mechanical and Mechatronic Engineering, University of Sydney, Camperdown, NSW 2050, Australia, <sup>d</sup>Priority Research Centre for Organic Electronics, University of Newcastle, Callaghan, NSW 2308, Australia, and <sup>e</sup>Department of Physics, University of Surrey, Guildford, Surrey GU2 7XH, United Kingdom.

\*Correspondence e-mail: marcop@uow.edu.au

Spatially fractionated ultra-high-dose-rate beams used during microbeam radiation therapy (MRT) have been shown to increase the differential response between normal and tumour tissue. Quality assurance of MRT requires a dosimeter that possesses tissue equivalence, high radiation tolerance and spatial resolution. This is currently an unsolved challenge. This work explored the use of a 500 nm thick organic semiconductor for MRT dosimetry on the Imaging and Medical Beamline at the Australian Synchrotron. Three beam filters were used to irradiate the device with peak energies of 48, 76 and 88 keV with respective dose rates of 3668, 500 and 209 Gy s<sup>-1</sup>. The response of the device stabilized to 30% efficiency after an irradiation dose of 30 kGy, with a 0.5% variation at doses of 35 kGy and higher. The calibration factor after pre-irradiation was determined to be 1.02 ± 0.005 µGy per count across all three X-ray energy spectra, demonstrating the unique advantage of using tissue-equivalent materials for dosimetry. The percentage depth dose curve was within ±5% of the PTW microDiamond detector. The broad beam was fractionated into 50 microbeams (50 µm FWHM and 400 µm centre-to-centre distance). For each beam filter, the FWHMs of all 50 microbeams were measured to be 51 ± 1.4, 53 ± 1.4 and 69 ± 1.9 µm, for the highest to lowest dose rate, respectively. The variation in response suggested the photodetector possessed dose-rate dependence. However, its ability to reconstruct the microbeam profile was affected by the presence of additional dose peaks adjacent to the one generated by the X-ray microbeam. *Geant4* simulations proved that the additional peaks were due to optical photons generated in the barrier film coupled to the sensitive volume. The simulations also confirmed that the amplitude of the additional peak in comparison with the microbeam decreased for spectra with lower peak energies, as observed in the experimental data. The material packaging can be optimized during fabrication by solution processing onto a flexible substrate with a non-fluorescent barrier film. With these improvements, organic photodetectors show promising prospects as a cost-effective high spatial resolution tissue-equivalent flexible dosimeter for synchrotron radiation fields.



## 1. Introduction

Exposure to ionizing radiation using ultra-high dose rates has been shown to increase the differential response between normal and tumour tissue (Favaudon *et al.*, 2014). Termed the 'FLASH' effect by its authors, ultra-high dose rates greater than 40 Gy s<sup>-1</sup> reported less normal tissue damage (Favaudon *et al.*, 2014). The first human patient was successfully treated with less than 200 Gy s<sup>-1</sup>, presenting lower skin toxicity and

similar tumour control compared with similar cases treated with conventional radiotherapy that delivers of the order of 6–12 Gy min<sup>-1</sup> (Bourhis *et al.*, 2019). The generation of such high dose rates can be very challenging for clinical linear accelerators that are commissioned in hospitals; therefore research is being conducted at synchrotron facilities that are capable of generating broad-beam synchrotron radiation at ultra-high dose rates (Wilson *et al.*, 2020). Synchrotron facilities are also capable of generating collimated beams at high dose rates with minimal beam divergence. The collimation of high-dose-rate X-rays into multiple microbeams is known as microbeam radiation therapy (MRT) and has shown promising results in animal studies with increased sparing of normal tissue compared with broad-beam irradiation (Slatkin *et al.*, 1992; Serduc *et al.*, 2009; Engels *et al.*, 2020). The development of MRT for clinical settings requires routine pre-treatment quality assurance to ensure treatment efficacy and patient safety. Such quality assurance can only be met by a strenuous protocol that directly measures and monitors the dose deposited during radiation treatment.

MRT employs quasi-parallel beams of low-energy X-rays. In contrast to conventional radiotherapy, MRT uses a tungsten carbide multi-slit collimator (MSC) to fractionate the beam spatially into rectangular blades 50 µm wide ('peaks') separated by a centre-to-centre distance of 400 µm, named 'valleys'. The beam height is approximately 500 µm and it is 2 cm wide, so in order to achieve a field size of 2 cm × 2 cm the target is moved vertically through the beam. The total dose deposited is then the sum of the radiation accumulated during the whole scan (Duncan *et al.*, 2020). Therefore, prior to MRT delivery, it is imperative that the spatial fractionation of the radiation field is verified and the peak-to-valley dose ratio (PVDR) is accurately quantified. The irradiation geometry must be reconstructed with a detector that has a high spatial resolution with an active volume of the order of 25 × 10<sup>-3</sup> mm<sup>3</sup> or less. The detector must also possess a strong radiation tolerance in order to be used during exposure to the hundreds of gray delivered during MRT. Such a combination of high spatial resolution and radiation tolerance introduces dosimetric challenges that cannot be met by the current standard of detectors (Ashraf *et al.*, 2020). Film is known for its high spatial resolution, allowing it to measure individual microbeams. However, two scans are required to reconstruct the peak and valley doses separately (Bartzsch *et al.*, 2015). In combination with the development time (approximately 24 h or more), film lacks the ability to be used for real-time feedback and can only be used for reference conditions. Like film, PTW microDiamond also has a high spatial resolution. PTW microDiamond can be used in edge-on orientation and positioned either in a valley or in a peak to measure separately the valley or peak dose, respectively, while the treatment is delivered by sweeping the tumour volume through the beam as described by Duncan *et al.* (2020) The electronic readout allows the microDiamond dosimeter to be used for real-time dosimetry, but these devices are highly dependent on the alignment methodology used. The alignment is very time consuming and, if unsuccessful, can result in significant errors

for dose calculations. Each device must be characterized in terms of its dose rate and energy dependence for kilo-electronvolt X-ray beams, which have also been shown to be dependent on the device geometry for different micro-Diamond models (Livingstone *et al.*, 2016). Silicon strip detectors have a high spatial resolution to resolve the microbeam in edge-on mode (Fournier *et al.*, 2017; Duncan *et al.*, 2020). However, misalignment issues with this device geometry setup have reported an over-estimation of the FWHM. Alterations in its device geometry are currently being investigated to increase its spatial resolution and radiation hardness (Davis *et al.*, 2018).

To overcome these limitations, we are investigating an organic semiconducting photodetector. Organic semiconductors take advantage of all the dosimetric and mechanical benefits of film, but without their limitations in the readout technique (Griffith *et al.*, 2020). Given their density (1 g cm<sup>-3</sup>) and hydrogen/carbon-based composition, organic semiconductors can mimic the dose of ionizing radiation deposited in water, reducing the need for complicated calibration factors and without perturbing the scattering conditions of the beam (Posar *et al.*, 2021). Organic semiconductors have shown promising results during investigations for application in medical imaging (Keivanidis *et al.*, 2008), light-emitting diodes (Hirata & Shizu, 2016) and advanced radiation dosimeters (Kingsley *et al.*, 2009; Mills *et al.*, 2013). However, there is an apparent lack of knowledge towards their sensitivity and tolerance to high-dose-rate ionizing radiation. We have previously exposed our organic photodetectors to kilo electronvolt and mega electronvolt photon beams in clinically relevant conditions, produced by a medical linear accelerator (Posar *et al.*, 2020a,b). However, there is currently no prior investigation into the response of organic semiconductors in synchrotron fields. This work is an important step towards high spatial resolution tissue-equivalent dosimetry for MRT.

## 2. Methods

The organic photodetectors (OPDs) were fabricated by ISORG (Grenoble, France) and consist of a 500 nm thick substrate with a 4.91 mm<sup>2</sup> active area. The sensitive volume features a fullerene acceptor and polymer donor bulk heterojunction, sandwiched between an indium tin oxide transparent top contact and a back contact attached to a gold pad. The photodetector was covered with a thick barrier film (polyethylene) and mounted onto a 1.5 mm thick printed circuit board (PCB) connected to a Kapton probe for signals routing. A single-channel electrometer and data acquisition system, X-TREAM, was used to read out the radiation-induced photocurrent in the OPDs (Petasecca *et al.*, 2012).

Measurements were conducted on the Imaging and Medical Beamline (IMBL) at the Australian Synchrotron (AS). A 3 T wiggler magnetic field was applied to the electron beam to produce synchrotron radiation, with experiments performed in hutch 2B located 32 m away from the wiggler source. The beam was shaped with a beam-defining aperture height ( $z$ ) of

**Table 1**

Beam properties for 3 T pink beam with 1.052 mm beam-defining aperture height and 20 cm × 20 cm field size using a PTW type 31014 PinPoint chamber at 10 mm s<sup>-1</sup> scan speed under reference conditions.

Filter name	Peak energy (keV)	Dose rate (Gy s <sup>-1</sup> )	Absolute dose deposited (Gy)
Cu–Cu	87.5	209	23
Cu–Al	76.2	500	54
Al–Al	47.8	3668	397

1.052 mm and width of 30 mm. The X-ray flux and average energy of the beam were varied via beam hardening using a combination of copper (Cu) and/or aluminium (Al) filters, producing what are referred to as ‘pink’ beams. The use of filters to alter the beam characteristics are outlined in Table 1, with a full description of the beamline components provided by Stevenson *et al.* (2017) and Livingstone *et al.* (2018).

All detectors were placed in a water-equivalent poly(methyl methacrylate) (PMMA) phantom of dimensions 15 cm × 15 cm × 10 cm with reference conditions defined for a 20 mm × 20 mm field size, with the detector positioned at a depth of 20 mm and 80 mm of backscatter (Livingstone *et al.*, 2017).

The absolute doses measured with the PTW PinPoint under reference conditions were corrected to consider pressure, temperature and polarization conditions. Peak and average energy parameters were extracted from Livingstone *et al.* (2018).

### 2.1. Radiation damage

The effects of radiation damage in the OPD were tested using the broad pink beam at the IMBL. The OPD was set up face-on (device surface perpendicular to the beam) under reference conditions and scanned vertically through the beam. An Al–Al filter was used to characterize the variation in charge accumulated by the device up to 40 kGy in steps of 5 kGy. The response was tested after each irradiation step by repeating the same exposure scan of the target used for calibration under reference conditions.

### 2.2. Relative dosimetry in broad beam

A calibration was performed with broad-beam irradiation for the pristine and pre-irradiated OPDs to perform relative dosimetry. Their response was calibrated with a pinpoint (PTW 31014) ionization chamber (IC), with the dependence of the IC to dose rate, temperature, pressure and polarity corrected for by the appropriate correction factors (Livingstone *et al.*, 2018). The calibration was achieved for a reverse bias of 3 V for all beam filter configurations and device orientations.

The response of the OPDs as a function of absolute dose deposited was achieved for two reverse bias configurations, 3 V and 10 V, for the Cu–Cu beam filter configuration. The dose deposited was increased by varying the scan speed between 1 and 20 mm s<sup>-1</sup> under reference conditions.

The ability of the OPDs to measure the dose delivered for clinical use was tested and compared with a calibrated PTW microDiamond. Both devices were positioned face-on and scanned vertically through the broad beam at solid water depths between 5 and 70 mm to create a depth dose profile for all filter configurations. The microDiamond was read out using a webline dosimeter/electrometer at no bias, as suggested by the manufacturer and the protocol adopted at IMBL, while the radiation-induced photocurrents from the OPDs were measured using the X-TREAM system with a reverse bias of 3 V, with both datasets normalized to a depth of 20 mm. All the measurements were repeated three times to obtain an average and an uncertainty, defined as one standard deviation.

### 2.3. Microbeam profile characterization

A tungsten multi-slit collimator (MSC) was inserted into the beam to spatially fractionate the broad beam into 50 microbeams all with a 50 μm FWHM and 400 μm centre-to-centre (c-t-c) distance (Livingstone *et al.*, 2017). A silicon epitaxial single-strip detector (EPI-51r) was used to align the MSC and phantom in the centre of the microbeam profile according to the protocol established by Lerch *et al.* (2011).

The OPDs were aligned edge-on (device surface parallel to the beam) within the phantom to take advantage of the 500 nm thick sensitive volume. Z-axis rotational alignment was achieved using the DynMRT rotation stage. The OPD was scanned through the full microbeam profile at a scan speed of 4 mm s<sup>-1</sup> for all filter configurations and a custom script was used to calculate the parameters of interest for MRT, *i.e.* PVDR, FWHM and c-t-c distance.

### 2.4. Geant4 simulation

The effects of the packaging material surrounding the OPDs, specifically the polyethylene barrier film layered above the organic substrate and the PCB backing, were modelled in *Geant4*, an open-source Monte Carlo toolkit that simulates the passage of radiation through matter (Agostinelli *et al.*, 2003; Allison *et al.*, 2006, 2016). The most recent version of the *Geant4* toolkit at the time of writing (Version 10.6 patch 2) was used. Two physical quantities were calculated with the simulation: (i) energy deposited within the sensitive volume and (ii) number of visible photons incident on the sensitive volume generated by the packaging materials. Therefore, *G4EmStandardPhysics\_option4* and *G4OpticalPhysics* were activated to simulate all electromagnetic and optical processes (*Geant4* Collaboration, 2020; Arce *et al.*, 2021). The cut was set equal to 10 nm. The produced optical photons (2–3 eV) do not deposit energy in the medium in the simulation. Therefore, their contribution to the energy deposition was accounted for by recording the number of optical photons incident on the sensitive volume of the detector and multiplying each by its energy, assuming the sensitive volume absorbed all incident visible light. Once an optical photon was registered to be incident on the sensitive volume, the *fStopAndKill* command was invoked to ensure the optical photon was killed and not re-counted.

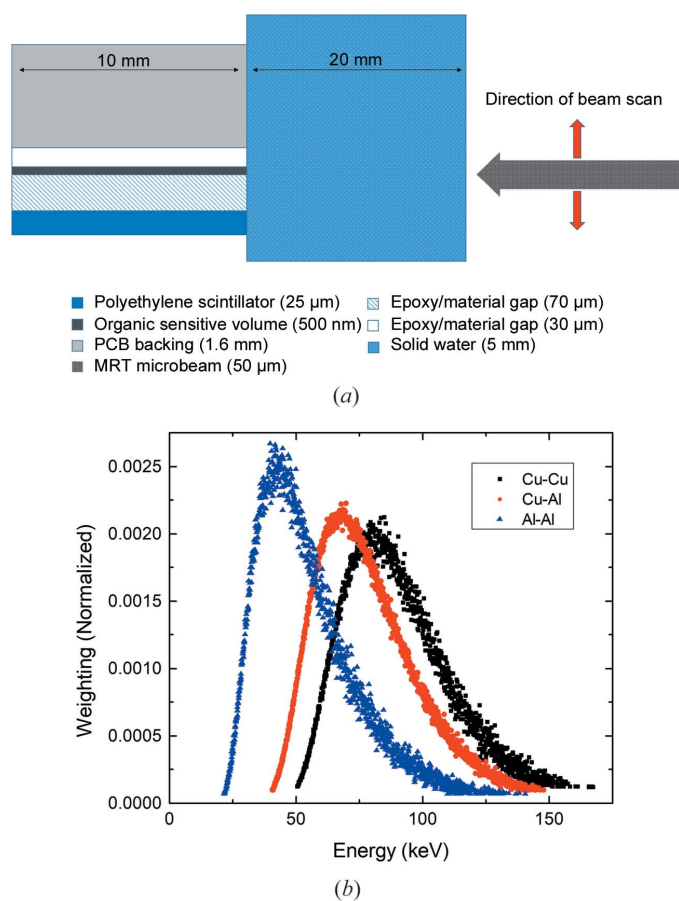


**Figure 1**  
(a) The detector geometry with beam direction and (b) the weighting distribution of the spectra at the IMBL for a 3 T wiggler field strength produced by the different filtration configurations [reproduced with permission from Dipuglia *et al.* (2019) under a Creative Commons Attribution 4.0 International License, <https://creativecommons.org/licenses/by/4.0/>] outlined in Table 1.

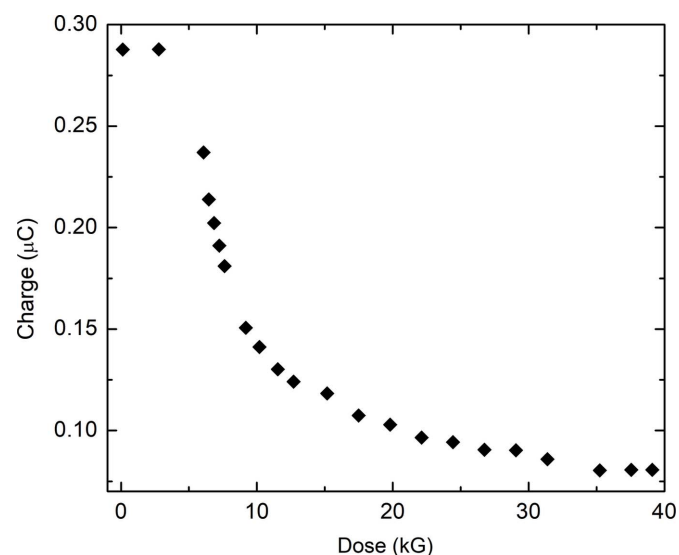


**Figure 2**  
The direct response of an organic photodetector to synchrotron radiation with an Al–Al filter configuration as a function of absorbed dose. Uncertainties are defined as one standard deviation and are smaller than the marker size.

A simplified detector geometry was constructed with five layers: 25  $\mu\text{m}$  polyethylene scintillator, 70  $\mu\text{m}$  epoxy resin/material gap, 500 nm organic semiconductor, 30  $\mu\text{m}$  epoxy resin/material gap and 1.6 mm PCB. Polyethylene naphthalene (PEN) was chosen as the plastic material for the simulation due to its common use for solar cell packaging. The detector was displaced 20 mm in solid water material in a PMMA phantom to mimic the experimental setup. A diagram of the detector setup and optical properties of each layer are presented in Fig. 1(a), and in Table S1 in the supporting information.

All three beam filters were simulated, matching the experimental beamline spectrum at the IMBL [as defined by Dipuglia *et al.* (2019)]. A graphical representation of the simulated spectra is provided in Fig. 1(b). The FWHM of the beam was set to 50  $\mu\text{m}$  and it was scanned across the detector for 600 beam positions to simulate the experimental procedure. Each run per beam position consisted of  $10^5$  histories and was repeated ten times with different simulation seeds to obtain an average and a statistical uncertainty defined as one standard deviation.

### 3. Results and discussion

#### 3.1. Radiation damage

Fig. 2 presents the response of the OPDs as a function of radiation damage induced by exposure to synchrotron radiation. Each point was calculated from the charge accumulated from one scan through the beam after exposure to the corresponding dose. The device efficiency decreased by approximately 30% after a cumulative irradiation dose of 30 kGy. At doses of 35 kGy or higher, the variation of any subsequent changes in charge output was observed to be  $<0.5\%$ , suggesting that the radiation effects stabilize past this point and the detector can be used in such high-dose-rate radiation fields for MRT applications. Our previous work has shown that such exposure to X-rays in the energy range of interest for MRT degrades the absorption spectrum of the acceptor and donor materials of the sensitive volume above wavelengths of 450 nm (Posar *et al.*, 2020b).

#### 3.2. Relative dosimetry in broad beam

The calibration factor was determined in the broad-beam configuration (without MSC spatial fractionation) for all three filter configurations, as shown in Fig. 3. The calibration factor for the pristine OPD was calculated to be  $0.53 \pm 0.027$   $\mu\text{Gy}$  per count. After exposure to 40 kGy of ionizing radiation the calibration factor increased to  $1.02 \pm 0.005$   $\mu\text{Gy}$  per count. The stability across all the energy spectra in Fig. 3 shows the unique advantage of using tissue-equivalent materials for dosimetry. The calibration factor only needs to be changed after prolonged exposure to ionizing radiation due to the radiation damage observed in Fig. 2. The larger uncertainty during exposure to the Al–Al beam filter configuration for the pristine OPD was due to the effects of radiation damage shown in Fig. 2. This beam filter configuration possessed the

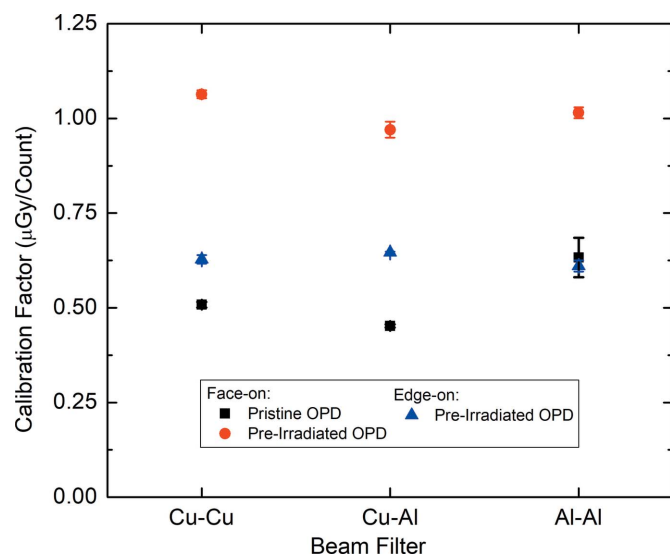


**Figure 3** The calibration factor for a pristine (black squares) and a pre-irradiated organic photodetector (red circles), both in face-on mode, and a pre-irradiated organic photodetector in edge-on mode (blue triangles). All measurements were achieved under reference conditions for a broad beam with filter configurations outlined on the x axis and calibrated with a PTW PinPoint IC.

largest dose rate, therefore producing substantial damage to the pristine OPD compared with the other filters. However, such effects stabilized at 35 kGy, suggesting that only one calibration factor would be required past this level for all energy spectra. Hence, the pre-irradiated OPD was chosen for edge-on characterization. Two different calibration factors were required to be calculated for each orientation of the device in response to the beam (face-on or edge-on). Further details are provided in Section 3.4. The calibration factor in edge-on mode was determined to be  $0.63 \pm 0.006 \mu\text{Gy}$  per count. The linearity of the OPD for the Cu–Cu filter, presented in Fig. 4, was observed for both reverse bias configurations, presenting an  $R^2$  value of 0.999 and sensitivities of  $164 \pm 0.8$  and  $398 \pm 0.4 \text{ pC Gy}^{-1}$  for reverse biases of 3 and 10 V, respectively. The higher electric field aids in reducing the trapping of the charge carriers, resulting in an increased carrier lifetime and therefore an increased sensitivity.

The broad-beam profile was measured as a function of depth within a solid water phantom. The pristine and pre-irradiated OPDs were compared with microDiamond as presented in Fig. 5. The over-response of the OPDs for depths greater than 20 mm is suggested to be due to two factors:

(i) Dose-rate dependence. We have previously shown that the OPDs are dose-rate dependent for conventional radiotherapy dose rates below  $60 \text{ Gy s}^{-1}$  during direct detection.

(ii) Fluorescence generated in the packaging. There is also a contribution of signal due to visible photons that are generated within the packaging material that are incident on the organic sensitive volume. This phenomenon will be investigated in a later section of this work and is suggested to be the reason for the greater percentage difference in depth dose curves of Cu–Cu with respect to Cu–Al, as shown in Figs. 5(a) and 5(b), respectively.

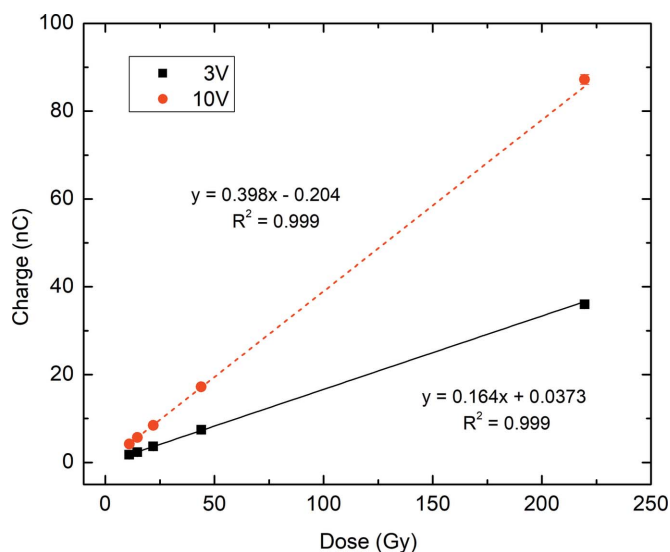


**Figure 4** The dose linearity for a pre-irradiated organic photodetector with applied reverse biases of 3 V (black squares) and 10 V (red circles) from a Cu–Cu beam filter configuration.

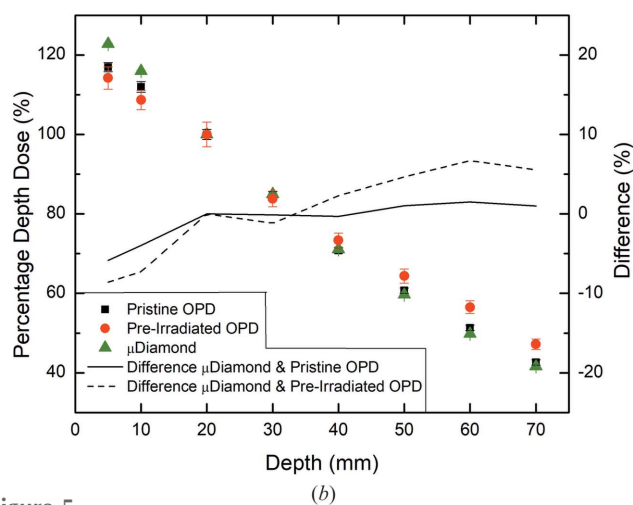
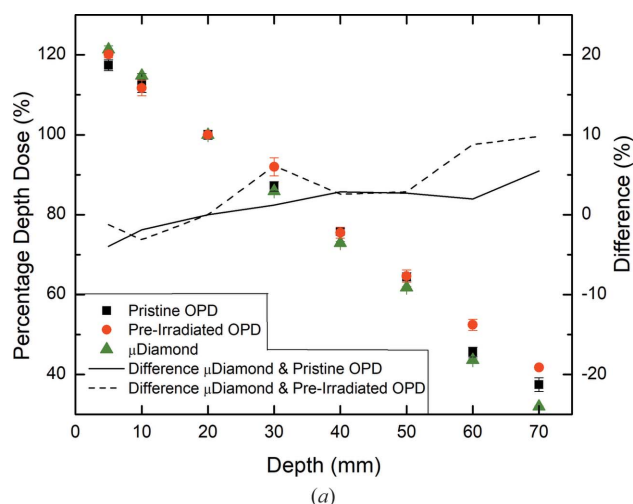


**Figure 5** Percentage depth dose curves measured by a pristine (black squares) and a pre-irradiated (red circles) organic photodetector with (a) a Cu–Cu and (b) a Cu–Al filter, with the percentage difference compared with microDiamond shown by green triangles.

**Table 2**

Summary of the microbeam profiles reconstructed using an organic photodetector in edge-on mode.

Values were determined from the average from all 50 microbeams with the error defined as one standard deviation.

Filter	FWHM ( $\mu\text{m}$ )	PVDR	c-t-c ( $\mu\text{m}$ )
Al–Al	$51 \pm 1.5$	$24 \pm 2$	$401 \pm 6$
Cu–Al	$52 \pm 1.4$	$8 \pm 0.6$	$404 \pm 7$
Cu–Cu	$69 \pm 1.9$	$6 \pm 0.4$	$404 \pm 5$

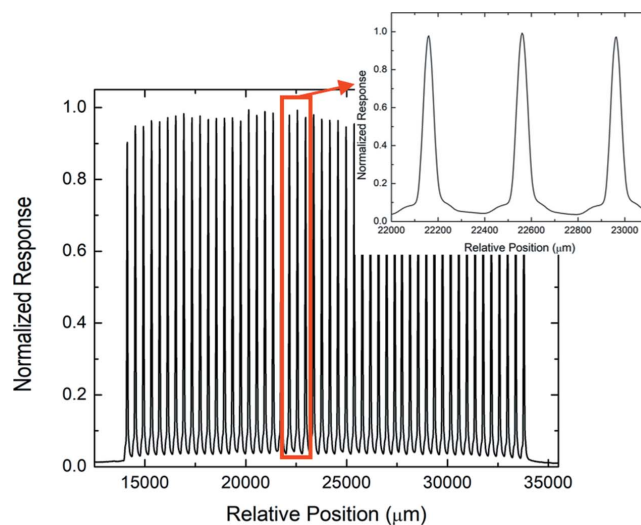
The pristine OPD was shown to be in the best agreement of 1% with microDiamond for depths greater than 20 mm, shown in Fig. 5(b). The deviation for the pre-irradiated OPD suggests that significant exposure to ionizing radiation has damaged the charge-transport mechanism in the sensitive volume, affecting its ability to accurately determine the dose deposited.

A comparison for depths less than 20 mm may not be significant due to the not-optimized packaging of the OPD for dosimetry. The packaging of the organic substrate on a PCB does not allow for a tight assembly of the device in the face-on orientation within the solid water phantom, leaving some air gaps laterally with respect to the position of the sensitive volume. This is likely to be the reason for a lack of scattering around the device at shallower depths which produce a signal under-responding by up to 5% with respect to the reference measurement.

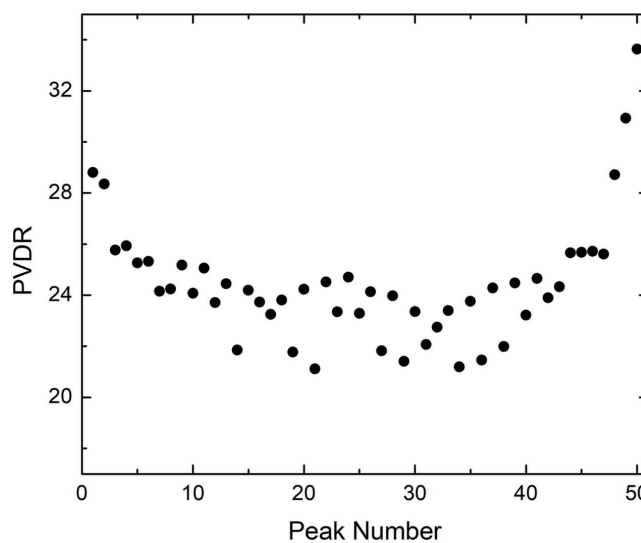
### 3.3. Microbeam profile characterization

The ability of OPDs to reconstruct microbeam profiles was evaluated for three filter configurations that altered the dose rate and peak energy of the beam, as outlined in Table 1. Despite the depth dose curves showing a more accurate response for the non-irradiated OPD, for the measurements of the profiles which all occur at the same depth in the phantom we adopted the pre-irradiated OPD which produced the more stable response observed in Fig. 2. The Al–Al filter scanned in Fig. 6 presented the expected reconstruction of the microbeam profiles compared with the scans in Figs. 7 and 8. Fig. 6(c) also produces the closest mean FWHM of  $51 \pm 1.4 \mu\text{m}$  and c-t-c distance of  $401 \pm 6 \mu\text{m}$  across the entire microbeam profile within the error of the physical fractionation. These results are in good agreement with the EPI,  $50.78 \pm 1.30 \mu\text{m}$ , and demonstrate better performance than many other dosimeters including fibre-optic dosimeters and the p-doped/n-doped/p-doped silicon planar junction strip detector (Davis *et al.*, 2018; Archer *et al.*, 2019). The error, defined as one standard deviation, is due to divergence of the beam, as shown by the convex/concave distribution of the PVDR/FWHM as a function of peak number.

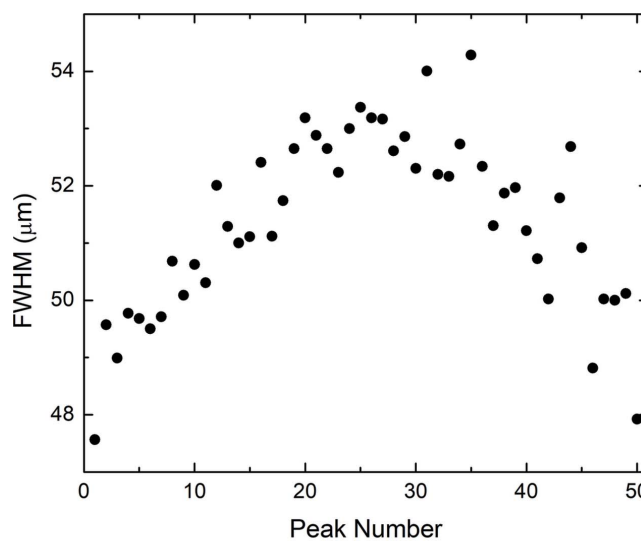
The PVDR and FWHM for the filter configurations with lower dose rates were less accurately determined, as shown in Table 2. While the c-t-c is within error, the FWHM increases from  $53 \pm 1.4 \mu\text{m}$  for the Cu–Al up to  $69 \pm 1.9 \mu\text{m}$  for the Cu–Cu which possessed the lowest dose-rate beam. Dose-rate dependence for direct detection of ionizing radiation has been shown for these devices for lower dose rates and may also be



(a)



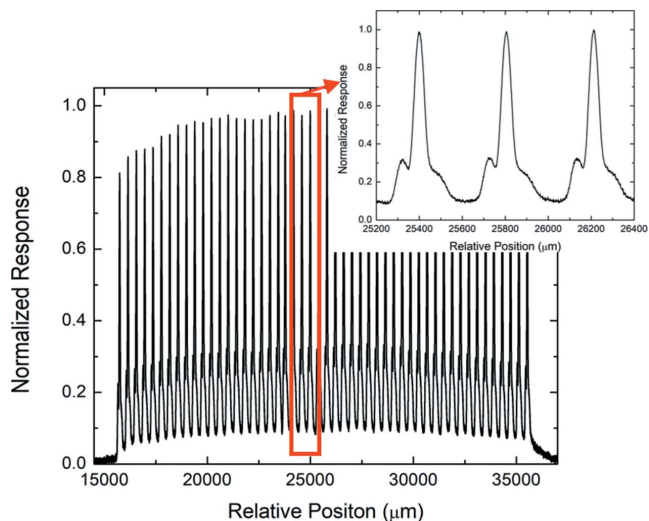
(b)



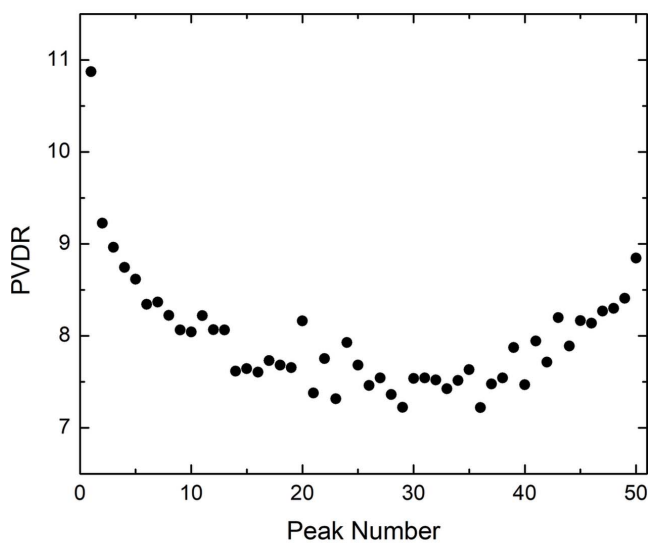
(c)

**Figure 6**

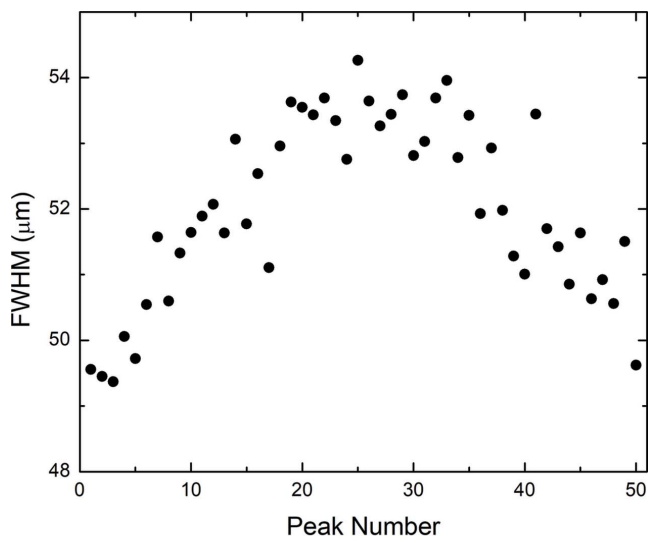
An organic photodetector in edge-on mode with Al–Al filtration (see Table 1), presenting (a) the 50 microbeam profile with an inset of three central microbeams, (b) PVDR and (c) FWHM.



(a)

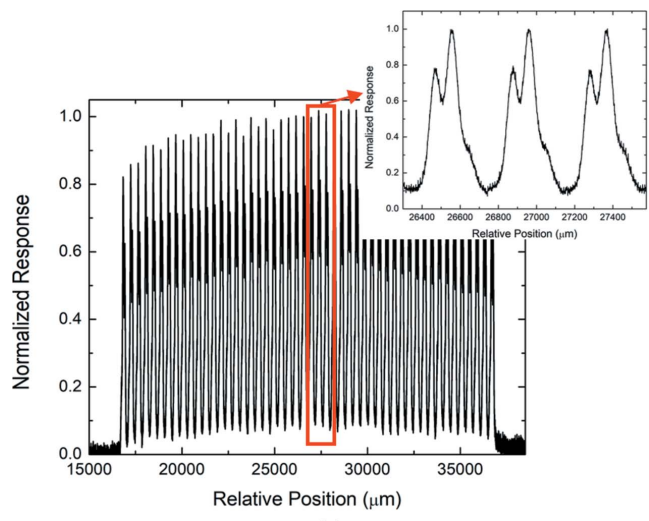


(b)

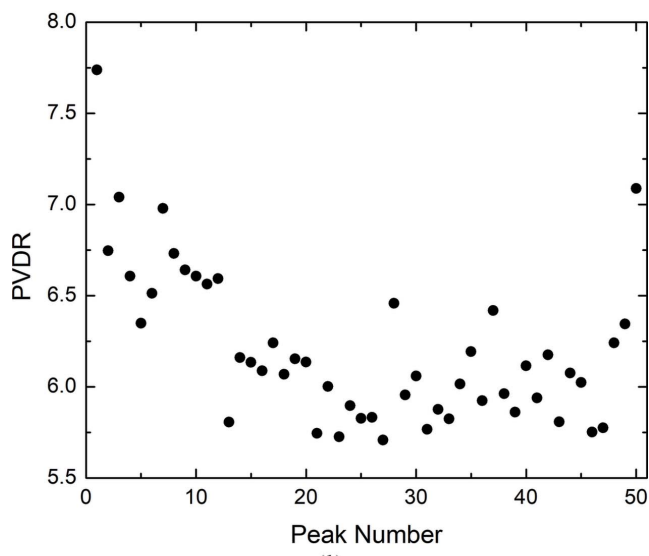


(c)

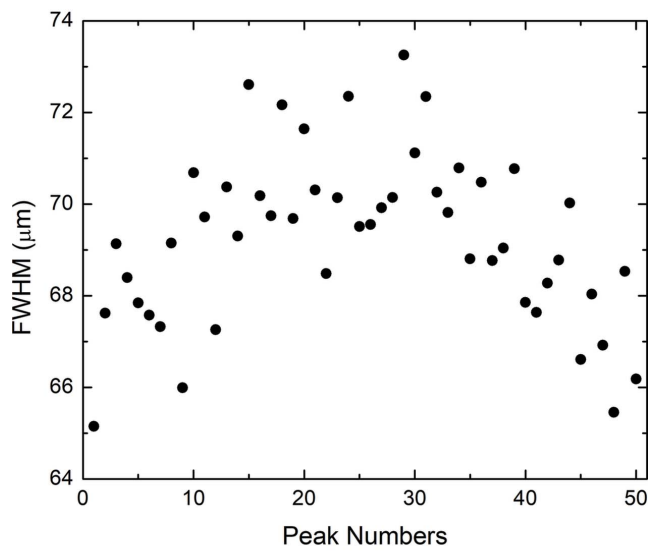
**Figure 7** An organic photodetector in edge-on mode with Cu–Al filtration (see Table 1), presenting (a) the 50 microbeam profile with an inset of three central microbeams, (b) PVDR and (c) FWHM.



(a)



(b)



(c)

**Figure 8** An organic photodetector in edge-on mode with Cu–Cu filtration (see Table 1), presenting (a) the 50 microbeam profile with an inset of three central microbeams, (b) PVDR and (c) FWHM.

suggested to be the reason for such divergence from the expected results (Posar *et al.*, 2020b).

The maximum photocurrent from the OPD for the Al–Al filter was  $100\times$  larger than that of the Cu–Al and Cu–Cu filters. However, it is obvious from the insets of the intrinsic scans in Figs. 7(a) and 8(a) that there is another phenomenon occurring. Firstly, the shape of one microbeam would ideally resemble a rectangular shape with a flat top. This shape has been shown for single-crystal diamond detectors (Livingstone *et al.*, 2016) but a more triangular shape was measured for the OPD. Secondly, and more evidently, is the appearance of side peaks surrounding the microbeam X-ray peak. Normalizing and aligning the central microbeam from all filter configurations in Fig. 9, a large second peak on one side of the microbeam and a large shoulder on the opposite side are observed. The peaks are suggested to be due to the packaging surrounding the sensitive volume of the OPD, which is sandwiched between a 1.5 mm thick PCB and 25  $\mu\text{m}$  thick polyethylene barrier film. These layers are proposed to be fluorescing when entering the beam, and the secondary optical photons generated by the interaction of the X-rays with the polyethylene film are subsequently being detected by the organic sensitive volume. This hypothesis was confirmed when the positioning of the peaks appeared on the opposing sides when the scan direction was reversed. From a comparison of the scan direction and orientation of the device in edge-on mode, it was determined that the large second peak was due to fluorescence of the polyethylene and the shoulder on the right-hand side was an effect of dose-response enhancement due to PCB scattering. A comparison of the peaks relative to the filtration suggests that the fluorescence of the packaging is strongly quenched at high dose rates and therefore has a less prominent effect on the higher flux of the Al–Al filtration, while the photocurrent response from the OPD was  $100\times$

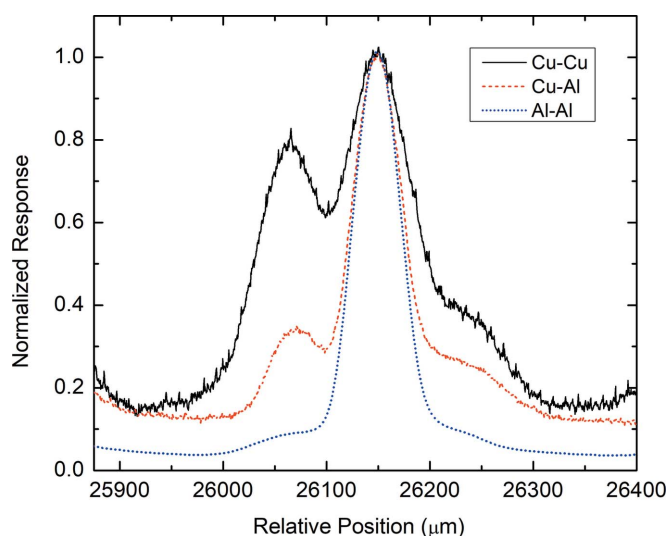


**Figure 9**  
The central microbeam measured using an organic photodetector in edge-on mode with Cu–Cu (solid black line), Cu–Al (dashed red line) and Al–Al (dotted blue line) filters, presenting the effect of the surrounding packaging on the ability to reconstruct the microbeam profile. Each series was normalized to its peak dose.

larger for the higher dose rate than for the lowest. The side peaks do not affect the calculation of the FWHM as the values were determined from a Gaussian fit. However, the side peaks broaden the FWHM and decrease the PVDR due to their influence on the valley region. Their influence is more apparent for the Cu–Cu filter configuration as the amplitude of the microbeam peak is comparable with the side peak. To validate this hypothesis a *Geant4* simulation was utilized.

### 3.4. *Geant4* simulation results

Barrier films are used to protect organic cells from environmental degradation. The most efficient and cost-effective barrier films are composed of polyethylene, which is known to possess a high scintillation performance with a deep-blue photon emission. Such blue wavelengths are also emitted from common plastic scintillators that are used as indirect radiation detectors for dosimetry (Nakamura *et al.*, 2011). Organic semiconductors have been coupled with plastic scintillators for applications in dosimetry, demonstrating their high sensitivity to these wavelengths (Posar *et al.*, 2020a). The effect of spurious light from the surrounding transparent material, similar to the polyethylene barrier film, is a well established phenomenon in scintillation fibre-optic dosimetry (Beddar *et al.*, 1992). The light generated in fibre-optic dosimetry glows blue and propagates perpendicular to the path of the beam. Since the OPD is positioned adjacent to the polyethylene layer with reference to the beam direction, any optical light travelling perpendicular to the beam would be incident on the sensitive volume before the OPD is in line with the beam. Therefore, we can suggest that the appearance of the side peak prior to the microbeam in Fig. 9 is due to the fluorescence of the polyethylene layer.

The *Geant4* simulation described in Section 2.4 was used to prove this hypothesis for all three filter configurations, presented in Fig. 10. The simulation showed that the polyethylene layer generated an abundance of visible photons that were incident on the sensitive volume. An additive layer, which has been suggested to be composed of an adhesive epoxy, created the separation of the side peak from the direct detection of the microbeam, suggesting that the additive material was unable to efficiently generate optical photons as easily as the polyethylene. The small shoulder located 50  $\mu\text{m}$  to the right of the microbeam peak, at the relative position of 26200  $\mu\text{m}$ , observed in Fig. 10 correlates with the PCB layer in Fig. 1(a). The shoulder was present during the scoring of the energy deposited by direct interaction with ionizing particles, suggesting that the PCB was generating secondary electrons due to the photoelectric and Compton effects that were detected by the sensitive volume. The small amplitude of the shoulder on the right-hand side of the microbeam peak indicates that only particles generated at the boundary of the PCB and sensitive volume were incident on the sensitive volume. The greater width of the shoulder on the right-hand side of the microbeam peak of the experimental data compared with the simulation suggests there was more scattering occurring

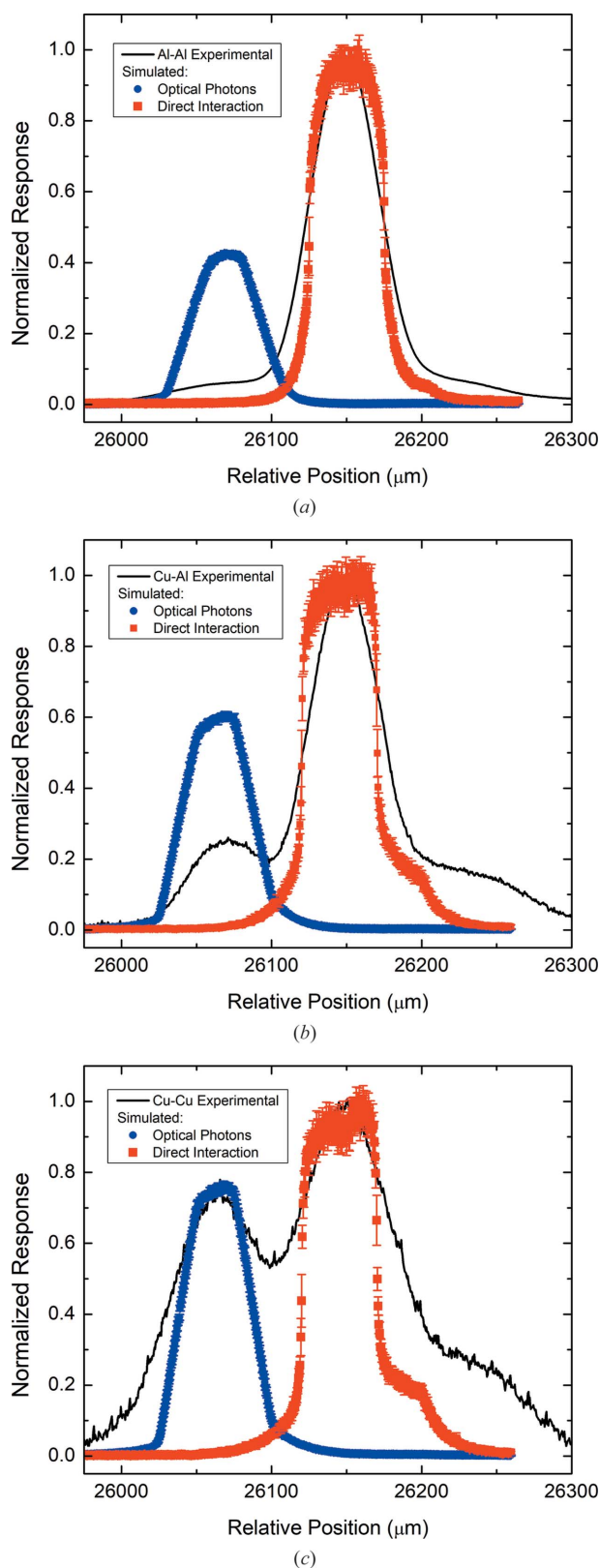


**Figure 10** Comparison of the experimental data and simulation results for (a) Al–Al, (b) Cu–Al and (c) Cu–Cu beamline filter configurations. The simulated results include the energy deposited from the direct interaction of the X-ray microbeam (red squares) and from optical photons generated by the barrier film (blue circles), which are then incident on the sensitive volume. Statistical uncertainties are defined as one standard deviation.

during the experiment than could be replicated during the simulation.

The relative amplitudes of the optical photon peak and the direct interaction with the X-ray microbeam match the experimental profile for the Cu–Cu beam filter, presented in Fig. 10(c). As expected from the experimental results, the relative amplitude of the optical peak decreases for the Al–Al beam filter. However, as shown in Fig. 10(a), the amplitude of the optical peak is situated at 43% with respect to the amplitude of the microbeam X-ray peak for the simulated data, compared with 5% for the experimental. The *Geant4* application developed and used in this work confirmed our hypothesis on the origin of the experimentally observed side peak but, at this stage, its results cannot be compared directly with the experimental data, as the quenching effect of the scintillator (Birks, 1964), optical losses between interfaces, charge transport in the organic detectors, the dose-rate dependence of the detector response and device efficiencies were not considered in the simulation. These parameters vary with energy spectra due to the different filters used, as outlined in Table 1, so the agreement of the simulated data with the experimental results varies with filter properties.

The *Geant4* simulation results support the hypothesis that the source of distortion in the reconstruction of the microbeam profiles is the result of visible photons generated in the barrier film. Unlike fibre-optic dosimeters, which are completely dependent on the use of optical fibre guides which are responsible for creating the spurious light, the packaging for the OPDs can easily be modified during the fabrication process by omitting any material capable of producing radioluminescence. Polyamide and Kapton are ideal replacements for the barrier film and PCB as they do not possess radioluminescence but are flexible substrates that can protect the device from environmental degradation. Thus, a modification of the packaging will remove both side peaks and improve the OPDs’ ability to reconstruct the microbeam profiles.

#### 4. Conclusions

This work is the first to explore the potential use of organic semiconducting photodetectors as dosimeters for synchrotron X-ray radiation. Their tissue-equivalence and extremely thin active area make them an ideal candidate for quality assurance in MRT, requiring only one calibration factor across various energy spectra. The response in such a harsh environment stabilizes to 30% efficiency after 30 kGy with a 0.5% variation up to 40 kGy. Depth dose curves are shown to be comparable with a microDiamond detector, within  $\pm 5\%$  error, which is acceptable in clinical radiotherapy. The over-response at larger depths is attributed to a dose-rate dependence. Synchrotron X-ray microbeams have been resolved with the detector, measuring an FWHM of  $51 \pm 1.4 \mu\text{m}$  for the Al–Al beamline filter configuration. *Geant4* simulations have proved that the microbeam dose profiles are distorted by radioluminescence of the packaging material. The problematic layers, specifically the barrier film and PCB, can easily be

replaced during fabrication to remove this phenomenon. The implementation of this optimization is currently being explored using Kapton substrates, to manufacture a new generation of organic photodetectors for MRT quality assurance.

## 5. Related literature

The following references, not cited in the main body of the paper, are cited in the supporting information: Bilki *et al.* (2020), Durmus *et al.* (2011), Hrostea *et al.* (2018), Kayaku Advanced Materials (2020), Stelling *et al.* (2017) and Wetzel *et al.* (2016).

## Acknowledgements

The authors thank the AS-IMBL team for the use of their facility and for assisting with the setup of the beamline. Thanks are also expressed to ISORG (Grenoble, France) for providing the samples tested in this work.

## Funding information

The following funding is acknowledged: Australian Government Research Training Program (scholarships to Jessie A. Posar and Matthew Large); Australian Institute of Nuclear Science and Engineering (awards to Jessie A. Posar and Matthew Large); NCMAS 2020 grant scheme of the National Computing Infrastructure; Imaging and Medical Beamline at the Australian Synchrotron, Australian Nuclear Science and Technology Organisation (award No. AS193/IMBL/15240).

## References

- Agostinelli, S., Allison, J., Amako, K., Apostolakis, J., Araujo, H., Arce, P., Asai, M., Axen, D., Banerjee, S., Barrand, G., Behner, F., Bellagamba, L., Boudreau, J., Broglia, L., Brunengo, A., Burkhardt, H., Chauvie, S., Chuma, J., Chytracsek, R., Cooperman, G., Cosmo, G., Degtyarenko, P., Dell'Acqua, A., Depaola, G., Dietrich, D., Enami, R., Feliciello, A., Ferguson, C., Fesefeldt, H., Folger, G., Foppiano, F., Forti, A., Garelli, S., Giani, S., Giannitrapani, R., Gibin, D., Gómez Cadenas, J. J., González, I., Gracia Abril, G., Greeniaus, G., Greiner, W., Grichine, V., Grossheim, A., Guatelli, S., Gumplinger, P., Hamatsu, R., Hashimoto, K., Hasui, H., Heikkinen, A., Howard, A., Ivanchenko, V., Johnson, A., Jones, F. W., Kallenbach, J., Kanaya, N., Kawabata, M., Kawabata, Y., Kawaguti, M., Kelner, S., Kent, P., Kimura, A., Kodama, T., Kokoulin, R., Kossov, M., Kurashige, H., Lamanna, E., Lampén, T., Lara, V., Lefebvre, V., Lei, F., Liendl, M., Lockman, W., Longo, F., Magni, S., Maire, M., Medernach, E., Minamimoto, K., Mora de Freitas, P., Morita, Y., Murakami, K., Nagamatsu, M., Nartallo, R., Nieminen, P., Nishimura, T., Ohtsubo, K., Okamura, M., O'Neale, S., Oohata, Y., Paech, K., Perl, J., Pfeiffer, A., Pia, M. G., Ranjard, F., Rybin, A., Sadilov, S., Di Salvo, E., Santin, G., Sasaki, T., Savvas, N., Sawada, Y., Scherer, S., Sei, S., Sirotenko, V., Smith, D., Starkov, N., Stoecker, H., Sulkimo, J., Takahata, M., Tanaka, S., Tcherniaev, E., Safai Tehrani, E., Tropeano, M., Truscott, P., Uno, H., Urban, L., Urban, P., Verderi, M., Walkden, A., Wander, W., Weber, H., Wellisch, J. P., Wenaus, T., Williams, D. C., Wright, D., Yamada, T., Yoshida, H. & Zschiesche, D. (2003). *Nucl. Instrum. Methods Phys. Res. A*, **506**, 250–303.
- Allison, J., Amako, K., Apostolakis, J., Araujo, H., Arce, P., Asai, M., Barrand, G., Capra, R., Chauvie, S., Chytracsek, R., Cirrone, G. A. P., Cooperman, G., Cosmo, G., Cuttone, G., Daquino, G. G., Donszelmann, M., Dressel, M., Folger, G., Foppiano, F., Generowicz, J., Grichine, V., Guatelli, S., Gumplinger, P., Heikkinen, A., Hrivnacova, I., Howard, A., Incerti, S., Ivanchenko, V., Johnson, T., Jones, F., Koi, T., Kokoulin, R., Kossov, M., Kurashige, H., Lara, V., Larsson, S., Lei, F., Link, O., Longo, F., Maire, M., Mantero, A., Mascialino, B., McLaren, I., Mendez Lorenzo, P., Minamimoto, K., Murakami, K., Nieminen, P., Pandola, L., Parlati, S., Peralta, L., Perl, J., Pfeiffer, A., Pia, M. G., Ribon, A., Rodrigues, P., Russo, G., Sadilov, S., Santin, G., Sasaki, T., Smith, D., Starkov, N., Tanaka, S., Tcherniaev, E., Tomé, B., Trindade, A., Truscott, P., Urban, L., Verderi, M., Walkden, A., Wellisch, J. P., Williams, D. C., Wright, D. & Yoshida, H. (2006). *IEEE Trans. Nucl. Sci.* **53**, 270–278.
- Allison, J., Amako, K., Apostolakis, J., Arce, P., Asai, M., Aso, T., Bagli, E., Bagulya, A., Banerjee, S., Barrand, G., Beck, B. R., Bogdanov, A. G., Brandt, D., Brown, J. M. C., Burkhardt, H., Canal, P., Cano-Ott, D., Chauvie, S., Cho, K., Cirrone, G. A. P., Cooperman, G., Cortés-Giraldo, M. A., Cosmo, G., Cuttone, G., Depaola, G., Desorgher, L., Dong, X., Dotti, A., Elvira, V. D., Folger, G., Francis, Z., Galoyan, A., Garnier, L., Gayer, M., Genser, K. L., Grichine, V. M., Guatelli, S., Guèye, P., Gumplinger, P., Howard, A. S. H. I., Hrivnáčová, I., Hwang, S., Incerti, S., Ivanchenko, A., Ivanchenko, V. N., Jones, F. W., Jun, S. Y., Kaitaniemi, P., Karakatsanis, N., Karamitros, M., Kelsey, M., Kimura, A., Koi, T., Kurashige, H., Lechner, A., Lee, S. B., Longo, F., Maire, M., Mancusi, D., Mantero, A., Mendoza, E., Morgan, B., Murakami, K., Nikitina, T., Pandola, L., Paprocki, P., Perl, J., Petrović, I., Pia, M. G., Pokorski, W., Quesada, J. M., Raine, M., Reis, M. A., Ribon, A., Ristić Fira, A., Romano, F., Russo, G., Santin, G., Sasaki, T., Sawkey, D., Shin, J. I., Strakovsky, I. I., Taborda, A., Tanaka, S., Tomé, B., Toshito, T., Tran, H. N., Truscott, P. R., Urban, L., Uzhinsky, V., Verbeke, J. M., Verderi, M., Wendt, B. L., Wenzel, H., Wright, D. M., Wright, D. M., Yamashita, T., Yarba, J. & Yoshida, H. (2016). *Nucl. Instrum. Methods Phys. Res. A*, **835**, 186–225.
- Arce, P., Bolst, D., Bordage, M., Brown, J. M., Cirrone, P., Cortés-Giraldo, M. A., Cutajar, D., Cuttone, G., Desorgher, L., Dondero, P., Dotti, A., Faddegon, B., Fedon, C., Guatelli, S., Incerti, S., Ivanchenko, V., Konstantinov, D., Kyriakou, I., Latyshev, G., Le, A., Mancini-Terracciano, C., Maire, M., Mantero, A., Novak, M., Omachi, C., Pandola, L., Perales, A., Perrot, Y., Petringa, G., Quesada, J. M., Ramos-Méndez, J., Romano, F., Rosenfeld, A. B., Sarmiento, L. G., Sakata, D., Sasaki, T., Sechopoulos, I., Simpson, E. C., Toshito, T. & Wright, D. H. (2021). *Med. Phys.* **48**, 19–56.
- Archer, J., Li, E., Davis, J., Cameron, M., Rosenfeld, A. & Lerch, M. (2019). *Sci. Rep.* **9**, 6873.
- Ashraf, M. R., Rahman, M., Zhang, R., Williams, B. B., Gladstone, D. J., Pogue, B. W. & Bruza, P. (2020). *Front. Phys.* **8**, 328.
- Bartzsch, S., Lott, J., Welsch, K., Bräuer-Krisch, E. & Oelfke, U. (2015). *Med. Phys.* **42**, 4069–4079.
- Beddar, A. S., Mackie, T. R. & Attix, F. H. (1992). *Phys. Med. Biol.* **37**, 925–935.
- Bilki, B., Bostan, N., Koseyan, O. K., Tiras, E. & Wetzel, J. (2020). *Turk. J. Phys.* **44**, 437–441.
- Birks, J. B. (1964). *The Theory and Practice of Scintillation Counting*. Oxford: Pergamon Press.
- Bourhis, J., Sozzi, W. J., Jorge, P. G., Gaide, O., Bailat, C., Duclos, F., Patin, D., Ozsahin, M., Bochud, F., Germond, J., Moeckli, R. & Vozenin, M. (2019). *Radiother. Oncol.* **139**, 18–22.
- Davis, J. A., Paino, J. R., Dipuglia, A., Cameron, M., Siegele, R., Pastuovic, Z., Petasecca, M., Perevertaylo, V. L., Rosenfeld, A. B. & Lerch, M. L. F. (2018). *Biomed. Phys. Eng. Expr.* **4**, 044002.
- Dipuglia, A., Cameron, M., Davis, J. A., Cornelius, I. M., Stevenson, A. W., Rosenfeld, A. B., Petasecca, M., Corde, S., Guatelli, S. & Lerch, M. L. F. (2019). *Sci. Rep.* **9**, 17696.

- Duncan, M., Donzelli, M., Pelliccioli, P., Brauer-Krisch, E., Davis, J. A., Lerch, M. L. F., Rosenfeld, A. B. & Petasecca, M. (2020). *Med. Phys.* **47**, 213–222.
- Durmus, H., Safak, H., Akbas, H. Z. & Ahmetli, G. (2011). *J. Appl. Polym. Sci.* **120**, 1490–1495.
- Engels, E., Li, N., Davis, J., Paino, J., Cameron, M., Dipuglia, A., Vogel, S., Valceski, M., Khochaiche, A., O’Keefe, A., Barnes, M., Cullen, A., Stevenson, A., Guatelli, S., Rosenfeld, A., Lerch, M., Corde, S. & Tehei, M. (2020). *Sci. Rep.* **10**, 8833.
- Favaudon, V., Caplier, L., Monceau, V., Pouzoulet, F., Sayarath, M., Fouillade, C., Poupon, M., Brito, I., Hupé, P., Bourhis, J., Hall, J., Fontaine, J. & Vozenin, M. (2014). *Sci. Transl. Med.* **6**, 245ra93.
- Fournier, P., Cornelius, I., Dipuglia, A., Cameron, M., Davis, J. A., Cullen, A., Petasecca, M., Rosenfeld, A. B., Bräuer-Krisch, E., Häusermann, D., Stevenson, A. W., Perevertaylo, V. & Lerch, M. L. F. (2017). *Radiat. Meas.* **106**, 405–411.
- Geant4 Collaboration (2020). *Physics Reference Manual*, [https://geant4.web.cern.ch/support/user\\_documentation](https://geant4.web.cern.ch/support/user_documentation).
- Griffith, M. J., Cottam, S., Stamenkovic, J., Posar, J. A. & Petasecca, M. (2020). *Front. Phys.* **8**, 22.
- Hirata, S. & Shizu, K. (2016). *Nat. Mater.* **15**, 1056–1057.
- Hrostea, L., Girtan, M., Mallet, R. & Leontie, L. (2018). *Mater. Sci. Eng.* **374**, 012015.
- Kayaku Advanced Materials (2020). *PMMA and Copolymer Technical Datasheet*. Version 2. Kayaku Advanced Materials, Westborough, Massachusetts, USA.
- Keivanidis, P. E., Greenham, N. C., Siringhaus, H., Friend, R. H., Blakesley, J. C., Speller, R., Campoy-Quiles, M., Agostinelli, T., Bradley, D. D. C. & Nelson, J. (2008). *Appl. Phys. Lett.* **92**, 023304.
- Kingsley, J. W., Pearson, A. J., Harris, L., Weston, S. J. & Lidzey, D. (2009). *Org. Electron.* **42**, 950–966.
- Lerch, M. L. F., Petasecca, M., Cullen, A., Hamad, A., Requardt, H., Bräuer-Krisch, E., Bravin, A., Perevertaylo, V. L. & Rosenfeld, A. B. (2011). *Radiat. Meas.* **46**, 1560–1565.
- Livingstone, J., Adam, J. F., Crosbie, J. C., Hall, C. J., Lye, J. E., McKinlay, J., Pelliccia, D., Pouzoulet, F., Prezado, Y., Stevenson, A. W. & Häusermann, D. (2017). *J. Synchrotron Rad.* **24**, 854–865.
- Livingstone, J., Stevenson, A. W., Butler, D. J., Häusermann, D. & Adam, J. F. (2016). *Med. Phys.* **43**, 4283–4293.
- Livingstone, J., Stevenson, A. W., Häusermann, D. & Adam, J. F. (2018). *Phys. Med.* **45**, 156–161.
- Mills, C. A., Chan, Y. F., Intaniwet, A., Shkunov, M., Nisbet, A., Keddie, J. L. & Sellin, P. J. (2013). *Phys. Med. Biol.* **58**, 4471–4482.
- Nakamura, H., Shirakawa, Y., Takahashi, S. & Shimizu, H. (2011). *EPL (Europhysics Lett)*, **95**, 22001.
- Petasecca, M., Cullen, A., Fuduli, I., Espinoza, A., Porumb, C., Stanton, C., Aldosari, A. H., Bräuer-Krisch, E., Requardt, H., Bravin, A., Perevertaylo, V., Rosenfeld, A. B. & Lerch, M. L. F. (2012). *J. Instrum.* **7**, P07022.
- Posar, J. A., Davis, J., Alnaghy, S., Wilkinson, D., Cottam, S., Lee, D. M., Thompson, K. L., Holmes, N. P., Barr, M., Fahy, A., Nicolaidis, N. C., Louie, F., Fraboni, B., Sellin, P. J., Lerch, M. L. F., Rosenfeld, A. B., Petasecca, M. & Griffith, M. J. (2021). *Adv. Mater. Technol.* <https://doi.org/10.1002/admt.202001298>.
- Posar, J. A., Davis, J., Brace, O., Sellin, P., Griffith, M. J., Dhez, O., Wilkinson, D., Lerch, M. L. F., Rosenfeld, A. & Petasecca, M. (2020a). *Phys. Imaging Radiat. Oncol.* **14**, 48–52.
- Posar, J. A., Davis, J., Large, M. J., Basiricò, L., Ciavatti, A., Fraboni, B., Dhez, O., Wilkinson, D., Sellin, P. J., Griffith, M. J., Lerch, M. L. F., Rosenfeld, A. & Petasecca, M. (2020b). *Med. Phys.* **47**, 3658–3668.
- Serduc, R., Bouchet, A., Bräuer-Krisch, E., Laissue, J. A., Spiga, J., Sarun, S., Bravin, A., Fonta, C., Renaud, L., Boutonnat, J., Siegbahn, E. A., Estève, F. & Le Duc, G. (2009). *Phys. Med. Biol.* **54**, 6711–6724.
- Slatkin, D. N., Spanne, P., Dilmanian, F. A. & Sandborg, M. (1992). *Med. Phys.* **19**, 1395–1400.
- Stelling, C., Singh, C. R., Karg, M., König, T. A. F., Thelakkat, M. & Retsch, M. (2017). *Sci. Rep.* **7**, 42530.
- Stevenson, A. W., Crosbie, J. C., Hall, C. J., Häusermann, D., Livingstone, J. & Lye, J. E. (2017). *J. Synchrotron Rad.* **24**, 110–141.
- Wetzel, J., Tiras, E., Bilki, B., Onel, Y. & Winn, D. (2016). *J. Instrum.* **11**, P08023.
- Wilson, J. D., Hammond, E. M., Higgins, G. S. & Petersson, K. (2020). *Front. Oncol.* **9**, 1563.